

# FEASIBILITY ASSESSMENT OF SPINNING CYLINDER LIFT FOR REMOTE FLIGHT IN MARS AND TITAN ATMOSPHERES

Marco Principi\*, Simon Prince\*\*

\*City University London UK, \*\*Cranfield University, UK

## Abstract

*A study is presented that aims to assess the feasibility of employing a spinning cylinder lifting assembly, instead of a conventional high lift fixed wing, which makes use of the Magnus effect to provide the lifting force for a micro-UAV vehicle to explore the surface of the Planet Mars, and/or Saturn's moon, Titan.*

*It is shown that modern computational methods for the solution of the laminar unsteady Navier-Stokes equations can successfully capture the physical trends and magnitudes of the lift and drag, and the viscous flow physics associated with static and spinning cylinders in sub-critical Reynolds number crossflows. The method, applied to a spinning cylinder, at different surface to freestream velocity ratios, for a constant  $U=15\text{m/s}$  freestream in the Earth, Mars and Titan surface atmosphere conditions, suggests that a spinning cylinder lift based micro-UAV might be feasible as a vehicle for the exploration of the Titanian surface, but would not be feasible for similar application in the very rarefied atmosphere of Mars.*

## 1 Introduction

This paper presents some selected results from a study into the feasibility of using spinning cylinder lifting surfaces instead of fixed wing planes for application to autonomous micro UAV flight vehicles for Earth, Mars and Titan atmospheres. Recent work by Badalamenti [14] has demonstrated the feasibility of a spinning cylinder lift micro-UAV vehicle for application in the Earth's atmosphere. The question, then, is could such a lift generation philosophy be feasible for an autonomous flight exploration

vehicle in the Martian atmosphere, where gas density and pressure and temperature is extremely low, or for the Titan atmosphere, which has a mixture of higher pressure and density gas, but at very low temperature.

As a first step to answer this question it was decided to extend the computational assessment of the aerodynamics of the Badalamenti spinning cylinder experiments [15], to further validate the method, in its ability to capture the physical trends. The method was then used to simulate the aerodynamic characteristics of the same cylinder, moving with the same forward speed of 15m/s, but under ground level conditions in average equatorial atmospheres of Mars and Titan.

## 2 Spinning Cylinders in Cross-Flow and the Magnus Effect

### 2.1 The Magnus Effect

Perhaps the first person to recognize the effect that a body which is both translating in a fluid and rotating about its axis, experiences a force at right angles to the direction of its motion, was the artilleryman, Benjamin Robins in 1742 [1]. The effect is now generally identified with Gustav Magnus who undertook experimental measurements with a rotating brass cylinder in 1853 [2]. Lord Rayleigh [3] undertook the first theoretical study of the phenomena, investigating the curving flight of a spinning tennis ball in 1877, resulting in the well-known potential flow solution obtained by the superposition of a doublet and a uniform free-stream, together with a vortex filament. The theory predicts that the Magnus force increases linearly with vortex filament (circulation)

strength. Ludwig Prandtl et al [4] undertook a series of experimental studies with spinning cylinders in water flows, providing detailed visualisations of the flow around these bodies with varying spinning speeds.

Lafay [5, 6] performed a series of experimental studies around the same time as Prandtl and identified cylinder aspect ratio as an important parameter – the lower the aspect ratio the lower the lift coefficient for the same flow conditions and spinning speed. He was also the first to observe the inverse Magnus effect that can occur at low freestream to cylinder surface velocity ratio ( $\Omega$ ), whereby the Magnus force existed, for a short spinning speed range, in the opposite direction to that predicted by Magnus. Significant experimental testing programmes by Reid [7], Thom [8 – 12] and Swanson [13] confirmed these findings and provided much data on the effect of Reynolds number (based on cylinder diameter), cylinder aspect ratio and the effect of the addition of various sized end plate disks to reduce the three-dimensionality of the flows.

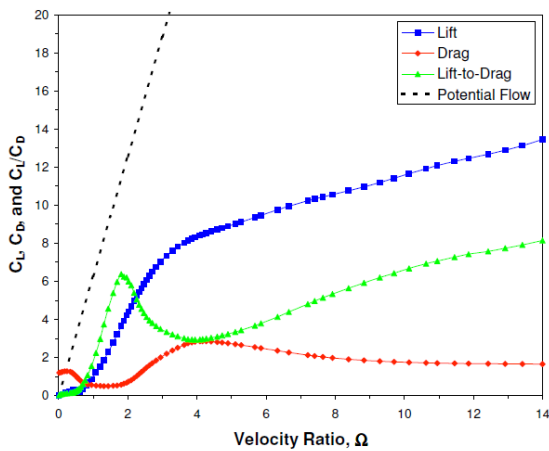
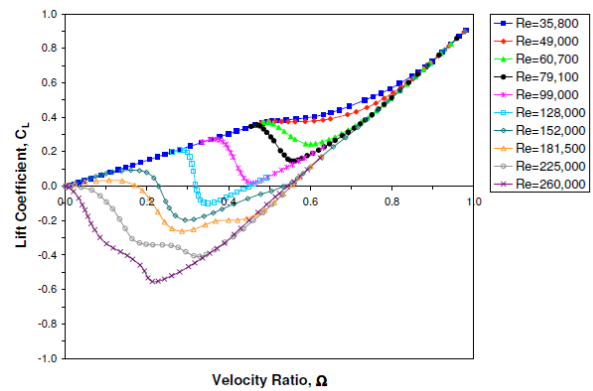
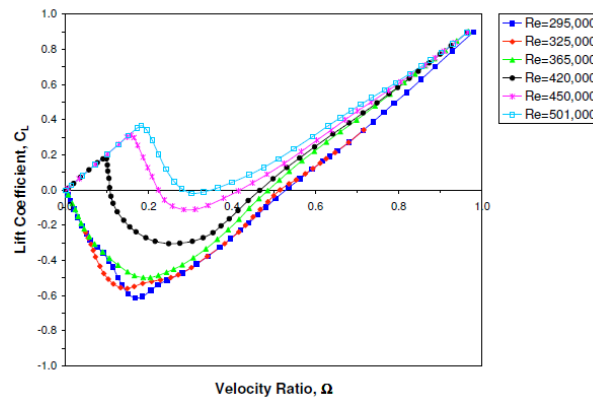


Fig 1: Swanson's experimental results for the lift and drag on a rotating cylinder in cross-flow [13].

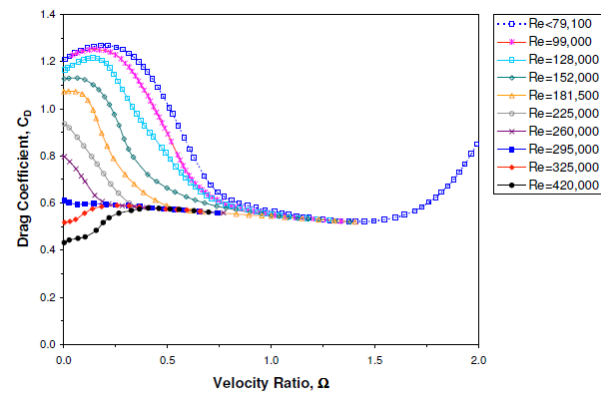
Fig. 1 presents experimental results typical of those obtained for spinning cylinders in crossflow, these being from Swanson's study. The lift coefficient is seen to rise slowly at very low spinning speed, but then begins to rise rapidly approaching  $\Omega$  of 1.0, and continues to rise without any evident stall effect, reaching a maximum of  $C_L$  of around 13 with a velocity ratio of 14.



a) Lift coefficient for subcritical Re.



b) Lift coefficient for critical and supercritical Re.



c) Drag coefficient.

Fig 2: Swanson's experimental results for the effect of Reynolds number on the lift and drag of a rotating cylinder in crossflow [13].

A typical value of  $C_{Lmax}$  for a wing with deployed high lift devices would be no more than 4, so  $C_L$  values of  $>10$  represent a significant performance enhancement over conventional high lift capable fixed wings. This means that a spinning cylinder lifting vehicle could carry significantly more load than an equivalent design fixed wing vehicle at the same flight speed – an important capability for a

micro UAV, particularly if low speed loiter is a requirement.

The variation of drag with  $\Omega$  is more complex, is less well understood, and very much depends on the Reynolds number, which governs the state of the boundary layers. Plotting the variation of lift to drag ratio reveals that, for this case, the maximum  $L/D$  is about 6, at a  $\Omega$  of around 2. This is a relatively low figure compared with a conventional wing design at low angle of attack, but this is not a surprise. It is suggested that drag could be reduced from the levels measured in the experimental studies to date, by the use of surface roughness. Results from other studies have revealed similar trends.

The inverse Magnus effect was found to be particularly sensitive to Reynolds number, as Swanson's data, presented in Fig 2, showed. Similar trends have also been revealed in many other experimental studies [5 – 14]. The inversion of the Magnus force tends to occur only for  $\Omega < 1$ .

An understanding of the physical mechanism giving rise to the Magnus force, and its inversion can only be obtained when considering the behavior of the viscous flow over the surface of the spinning cylinder. A schematic representation of the flow is given in fig 3.

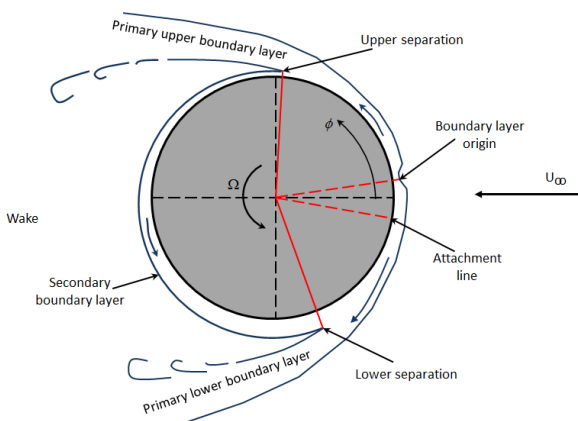


*Fig 3: Schematic representation of the viscous flow around a spinning cylinder in crossflow.*

For a non-spinning cylinder, the attachment line exists on the windward symmetry plane, and two separate boundary layers can be considered to be formed, both with

their origin on the attachment line. Assuming there are no significant roughness effects and the flow is not close to critical Reynolds number conditions (transitioning boundary layers), both boundary layers will separate at the same circumferential angle,  $\pm\phi$ , on the cylinder surface.

Once the cylinder begins to rotate, the boundary layer separation is shifted backwards on the side of the cylinder that is moving with the fluid (upper surface in fig 3), and is shifted further forwards on the side opposing the flow of the freestream (lower surface in fig 3). There is then a consequent change in surface pressure distribution, which is no longer symmetric, and, to a lesser extent, an asymmetric distribution of surface friction. The result is a net transverse force – the Magnus force, and the deflection of the wake.

At low Reynolds numbers (subcritical) when the boundary layers over the upper and lower cylinder surfaces are laminar, they both undergo laminar separations. In such circumstances the laminar shear layer on one, or both sides, can undergo transition and reattachment.

At higher Reynolds numbers (supercritical) when both boundary layers are fully turbulent, they both undergo turbulent separation. In between these states is the interesting regime in which the inverse Magnus effect occurs, which is when one boundary layer is in a different state to the other. The boundary layer on the upstream moving surface (lower surface in fig 3) usually undergoes transition prior to that on the downstream moving surface. The separation line associated with this transition will then tend to quickly move downstream exposing this surface to a much greater extent of suction. If this suction is great enough that it counteracts that on the opposing side, the Magnus force will be reversed. With higher Reynolds number, the opposite boundary layer will also undergo transition and its separation line undergo a shift downstream that will act to reduce the magnitude of the inverse Magnus force until a positive Magnus force is re-established.

This explanation is somewhat simplified, and it is true to say that the physical interactions

with many variables affecting the flow are so complex, that the process is still not fully understood.

## 2.2 Wake Shedding

A spinning cylinder behaves similarly to a static cylinder in crossflow at low spinning rates. The boundary layer separation from the upper and low surfaces causes the periodic shedding of large coherent vortical structures into the wake. The low frequency shedding has been found to occur with a Strouhal number,  $St$ , of between 0.15 and 2.0. Increasing  $\Omega$  induces several changes in the cylinder's wake, the most important of which are the narrowing and biasing of the wake (towards the side where the peripheral velocity and freestream velocity are in opposition); the creation of closed streamlines about the cylinder; and the eventual suppression of the periodic nature of the wake.

The physical mechanism for this shedding suppression is not exactly understood, but the literature is generally in agreement that, for all Reynolds numbers for which vortex shedding from a rotating cylinder occurs ( $Re \geq 47$ ), there is always a critical velocity ratio ( $\Omega_c$ ) beyond which shedding ceases. Between  $0 < \Omega < \Omega_c$ , vortices are formed and shed alternately from the two sides of the cylinder in much the same manner as for a stationary cylinder.

For spinning rates above  $\Omega_c$ , most studies report the shedding of a single vortex from the upstream moving wall of the cylinder (where the cylinder surface opposes the freestream), with no other vortices then being shed. The value of the critical velocity ratio is known to be a function of Reynolds number, with most studies indicating that  $\Omega_c$  increases with  $Re$  before reaching a constant value of  $\Omega_c \approx 2$  when  $Re \geq 200$ .

## 3 Modelling the Atmospheres

### 3.1 The Earth

The conditions for the Earth's atmosphere were assumed to be those at which the experiments of Badalamenti were performed. These are listed in table 1.

### 3.2 Mars

The atmosphere of Mars has been thoroughly measured by several landers and wheeled rover craft which have landed on Mars. The first of these was the US Viking lander in 1976. The Mars atmosphere is composed 95% Carbon Dioxide gas with traces of Nitrogen and Argon gas. For the purposes of this study it was assumed that it is 100%  $CO_2$ . The surface temperature varies seasonally and periodically according to the sol (Martian day) in the range 140 – 310K, with an average temperature of 215K, which was the value chosen for these calculations. The average surface pressure is 6.1 millibars, varying seasonally by about 30%. The average pressure was chosen in this study.

### 3.3 Titan

The atmosphere of Saturn's moon, Titan, was first sampled by the Huygens probe in 2005, which entered its atmosphere and successfully landed on its surface. Titan's atmosphere is composed of 98.4% Nitrogen gas, with traces of methane and hydrogen. For the purposes of this study it was assumed that it comprises 100%  $N_2$ . The surface pressure is about 1.45 times higher than that on Earth, being much denser, with an average surface temperature of only 94K.

Table 1 presents the assumptions and conditions used for the calculations, where the viscosity is calculated using Sutherland's law with the appropriate constants (assuming no sensitivity to pressure), the density via the perfect gas relation, and the Reynolds number, based on cylinder diameter, for a freestream speed of 15 m/s (the constant wind speed in the Badalamenti experiment). Also presented is the ratio of the surface gravitational acceleration constant to that for Earth,  $g/g_E$ , which is used to assess lifting capability in the analysis.

		Earth	Mars	Titan
Assumed Atmospheric constituents		Air	100% $CO_2$	100% $N_2$
Average surface conditions	$g/g_E$	1.000	0.387	0.138
	$\rho$ ( $kg/m^3$ )	1.1847275	0.0155	1.88
	$p$ (Pa)	101325	610	145000
	$T$ (K)	298	215	94
	$\gamma$	1.4	1.3	1.4
	$\mu$ (kg/ms)	$1.83 \times 10^{-5}$	$1.09 \times 10^{-5}$	$0.64 \times 10^{-5}$
Cylinder Reynolds No / D		$9.09 \times 10^4$	$0.19 \times 10^4$	$39.2 \times 10^4$

Table 1: Atmospheric conditions used in the present simulation study.

## 4 Investigation Methodology

### 4.1 The Experimental Test Case

This study first aimed to validate the computational simulation method by computing the unsteady viscous flow about the rotating cylinder tested in the wind tunnel study of Badalamenti [14]. Simulations were then performed for the same test case, but with the gas chemistry and atmospheric conditions changed to model the same flow at the surface of Mars and of Titan.

The cylinder in the Badalamenti study was of aspect ratio of 5.1, with external diameter  $D = 88.9\text{mm}$  and length  $b = 450\text{mm}$ . During the tests relevant to this work, the cylinder was fitted with two circular endplates in an attempt to minimize the three-dimensionality of the flow. The endplate-to-cylinder diameter ratio was 2.0, and the endplates were fixed to the end-plugs so that they spun with the cylinder. Each endplate was 2 mm thick and had a  $45^\circ$  chamfer over the outer 10 mm of the diameter. It is known that end plates are unable to fully enforce 2D flow behavior, and that there is generally strong sensitivity in both lift and drag to aspect ratio, and end plate size.

The data from the wind tunnel tests were those for a fixed wind speed of  $15\text{m/s}$  such that the Reynolds number based on diameter was fixed at  $9.1 \times 10^4$ . Force data was measured via an overhead 6 component balance

The fluctuating pressure field in the wake on the upstream moving wall side of the cylinder was traversed using three Kulite CTQH-187 series dynamic pressure transducers (rated at 5 psi). These signals were digitally sampled at a rate of 300 Hz, over a period of 60 s, and a fast Fourier transform (FFT) algorithm was used to transform the recorded pressure waveforms from the time domain to the frequency domain and so obtain the frequency power spectrum, which was used to obtain the dominant shedding frequency strouhal number.

### 4.2 The Numerical Method

A commercial CFD flow solver was employed to solve the Navier Stokes equations through an

explicit time marching, finite volume scheme, with nominally 3<sup>rd</sup> order accuracy in space and 2<sup>nd</sup> order accuracy in time assuming, a purely laminar flow. This assumption was assumed valid for the experimental case (Earth), and for Mars where the Reynolds numbers were clearly subcritical. For Titan the calculated Reynolds number of  $3.9 \times 10^5$  is high enough for the boundary layer to be transitional on the surface. For this case, however, only laminar boundary layer calculations were run in order to keep the computational cost as low as possible. Time steps of 0.1 milliseconds were employed, with convergence defined at five orders of residual convergence or 1000 iterations per time step.

Hybrid computational grids (unstructured outer grid with embedded structured boundary layer zone) were developed to resolve the quasi-3D flow over a 3D spanwise 250mm section (centre section of the experimental model cylinder) using periodic boundary conditions to model a quasi-infinite spanwise length cylinder. The cylinder surface used a prescribed circumferential slip velocity boundary condition.

Grid	Number of Cells
Fine	3,280,000
Intermediate 1	1,200,000
Intermediate 2	606,000
Coarse	324,000

*Table 2: Computational grid sizes employed*

A grid sensitivity for three spinning cases for Earth conditions, were performed with grid sizes as given in table 2. The course grid is shown in fig 4. The first cell height adjacent to the cylinder surface was set at  $1 \times 10^{-5}D$  for all grids, giving about 30 cells in the attached laminar boundary layers for the fine grid case.

Data for lift and drag for the 1.2 million cell grid was found to match those obtained on the 3.28 million cell grid to within 2%, providing confidence that the force data for the finest mesh results could be regarded as grid converged. It was therefore decided to use the fine 3.2 million cell grid as the baseline grid for the study. All of the results presented in this paper are derived from this grid. Calculations at

different spinning speeds were undertaken over the range,  $0 > \Omega > 3.0$ .

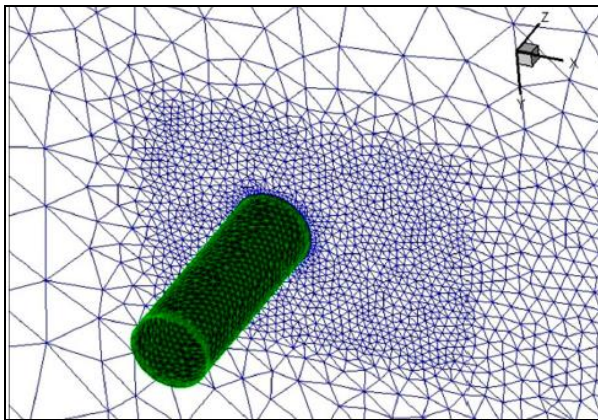


Fig 4: Computational surface grid (green) and the left hand periodic plane (blue) for the course grid.

The data processing software, SPIKE, was used to compute the Fast Fourier Transform (FFT) of a large enough sample (a minimum of 5 seconds worth of data following stabilization of the signal) of computed lift and drag signals in order to analyse the frequency of vortex shedding, for an FFT size of 2048, using the Hanning window.

## 5 Results and Discussion

### 5.1 Simulations for Earth Atmosphere, $Re_D=9.1 \times 10^4$

Fig. 5 presents the comparison of the computed lift coefficient with the experimentally measured averaged data of Badalamenti, where the maximum and minimum  $C_L$  predicted in the unsteady flow for each spinning speed are denoted by the red whiskers. The numerical predictions appear to match the experimental measurements very well in the range  $0.5 > \Omega > 1.5$ . At lower spinning speeds, the experimental data appears to sit around the level of the maximum predicted in the numerical simulations, though these are very close to zero. In particular, the simulation did not seem to capture the significant reduction in  $C_L$  that

appeared in the experimental trend at around  $\Omega = 0.5$ , although the averaged  $C_L$  data did resolve very small negative lift (inversed Magnus effect) for  $0.05 < \Omega < 0.4$ . While the general trend in increasing  $C_L$  with increasing  $\Omega$  is correctly resolved, the simulated average  $C_L$  for the two spinning speeds  $\Omega = 2.0$  and  $3.0$ , is seen to be up to 20% below the measured average value.

Fig 6 compares the measured and predicted variation of average (and minimum and maximum instantaneous values for the simulated data) drag coefficient. The magnitude of the numerically predicted drag would not be expected to match the experimental results as the experimental cylinder was of finite aspect ratio, and hence would be affected by induced drag, while the infinite span computed data would capture no such effect. A separate set of “corrected” numerical data has been added, where the curve has simply been shifted up to match the drag for the static cylinder to account for the induced drag increment. It can be seen that the predicted trends match the experimental ones reasonably well up to  $\Omega = 2.0$ , above which the experimental measurement shows a significant rise to a high value at  $\Omega = 3.0$ . The corresponding rise in computed drag is only modest.

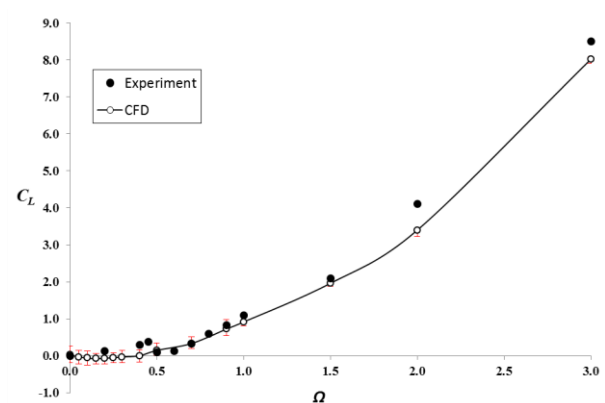


Fig 5: Variation of  $C_L$  with  $\Omega$  for Earth surface conditions.  $U = 15$  m/s.

Fig 7 presents the comparison between the measured wake shedding Strouhal number with that captured in the numerical simulations. The agreement between experimentally

measured and numerically resolved shedding frequency appears to be very good at  $\Omega < 1.0$ . The rate at which  $St$  increases with spinning speed, above  $\Omega = 1.0$ , is under-predicted by the simulation. However, the numerical simulations did successfully capture the suppression of wake eddy shedding above  $\Omega = 1.5$ , and its disappearance above  $\Omega = 2.0$ .

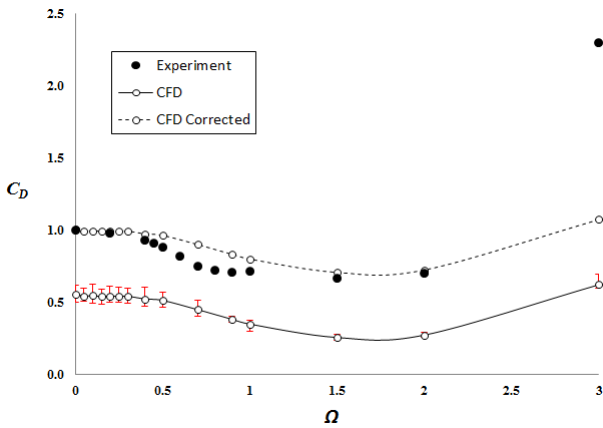


Fig 6: Variation of  $C_D$  with  $\Omega$  for Earth surface conditions.  $U = 15$  m/s.

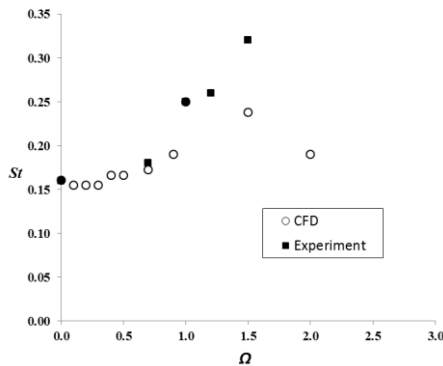


Fig 7: Variation of wake shedding Strouhal number with  $\Omega$  for Earth surface conditions.  $U = 15$  m/s.

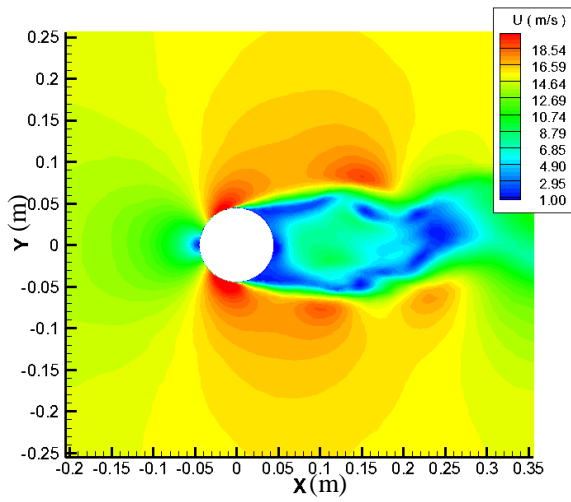
The contours of instantaneous velocity magnitude at  $C_{Lmax}$  on the cylinder spanwise centre-plane, at a selection of the spinning speeds, are presented in fig 8. The large wake with embedded vortical structures is clearly seen for the static cylinder case, where the velocity field close to the cylinder surface appears quite symmetric about the  $y = 0$  axis. This explains why even  $C_{Lmax}$  is very close to zero – the surface pressure distribution being close to a symmetric one. The only noticeable

difference that develops as spinning speed is increased appears to be a slight narrowing of the wake. Close scrutiny of the computed boundary layer profiles up to separation confirms that the boundary layer state is laminar on both sides, which is to be expected for this subcritical Reynolds number case. At  $\Omega = 1.0$ , a considerable asymmetry in the lobes of accelerated velocity is evident, which will result in a much larger extent of surface suction on the lower surface (in this case) than on the upper surface. The lower surface separation location is seen to be noticeably further leeward than that on the upper surface. This is the cause of the Magnus force in the negative  $y$  direction. In addition the viscous wake is seen to be considerably narrower.

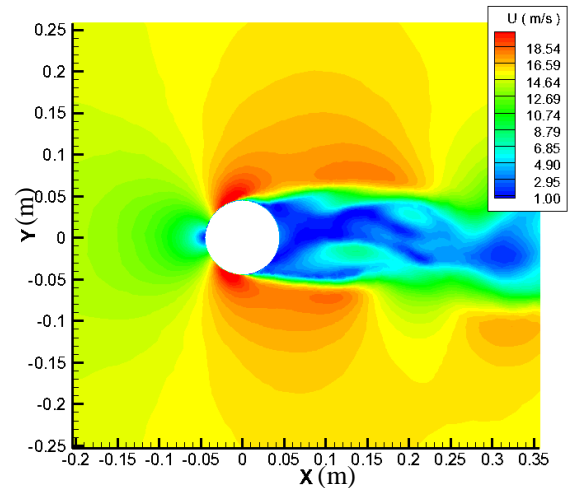
At  $\Omega = 2.0$ , both the forward attachment line and the wake are seen to be shifted towards the upper surface, with the wake being deflected upwards. The wake has also been closed and is now very small in streamwise extent, and scrutiny of the variation of this flow in time reveals very little large scale fluctuation, confirming the findings from experiment that wake shedding is effectively suppressed by a spinning speed of  $\Omega = 2.0$ .

Fig 9 presents time resolved variation of computed  $C_L$  for  $\Omega$  of 0.0, 1.0 and 2.0. Averaging of all computed forces was done with the signal only following 1 second of flow time in order to allow any non-physical transients to die out prior to averaging. A significant level of unsteadiness in lift coefficient is evident at  $\Omega = 0.0$ , where the average lift is, as expected, zero. At  $\Omega = 1.0$  the average  $C_L$  is increased to nearly 1.0, while the level of unsteadiness is significantly reduced, and by  $\Omega = 3.0$  the average  $C_L$  is over 3.0 with only a very small level of fluctuation in the lift signal.

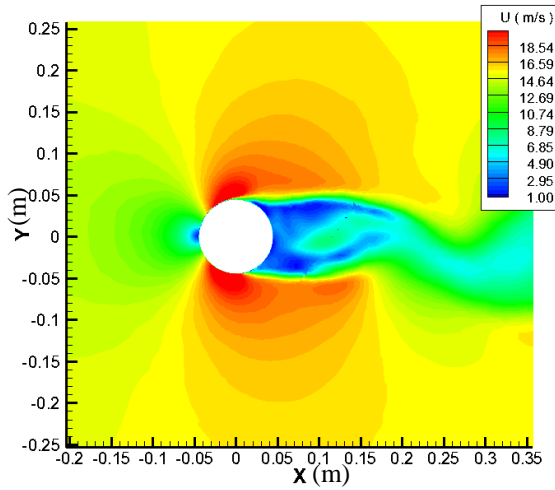
The agreement between the output from the computational model and experiment, for Earth atmosphere conditions, is suggested to be good enough, with the correct physical trends and force magnitudes captured, for one to be confident that the method should give the correct physical trends, and reasonable predictions of force magnitudes for a spinning cylinder in non-Earth conditions.



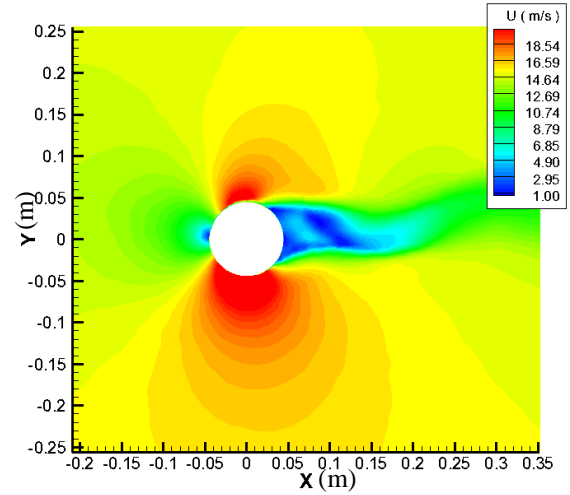
a)  $\Omega = 0.0$



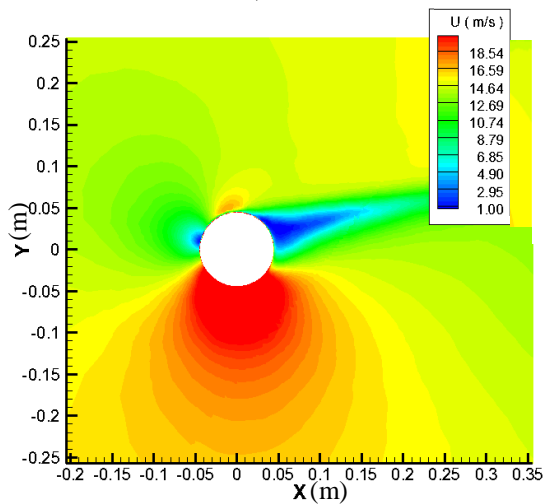
b)  $\Omega = 0.3$



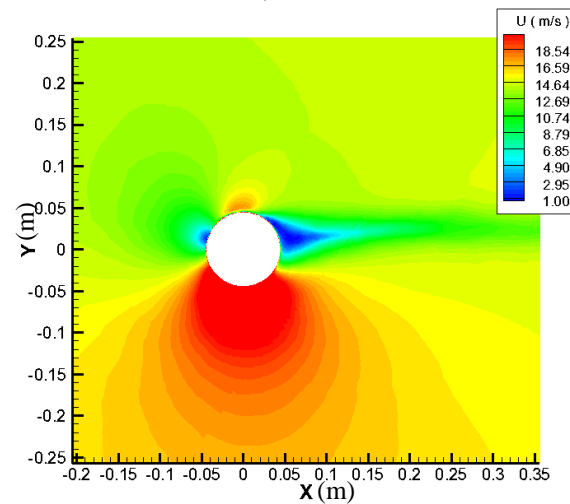
c)  $\Omega = 0.5$



d)  $\Omega = 1.0$



e)  $\Omega = 1.5$



f)  $\Omega = 2.0$

Fig 8: Instantaneous contours of velocity magnitude at  $C_{Lmax}$ . Earth surface conditions,  $U=15\text{m/s}$ .

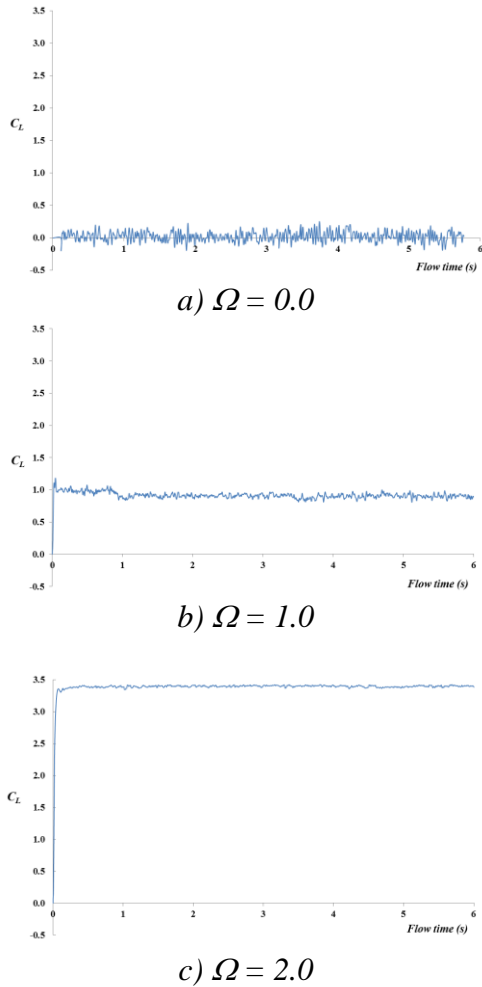


*Fig 9:  $C_L$  time histories for three spinning speeds. Earth surface conditions.  $U = 15\text{m/s}$ .*

#### 4.2 Simulations for Martian Atmosphere, $Re_D = 0.2 \times 10^4$

Figs 10 and 11 present the computed variation of the average lift and drag coefficients, together with indications (red vertical bars) of the corresponding maximum and minimum instantaneous values captured at any instant in the time history. For flight at the same forward speed in the ground level atmosphere on Mars, where the gas density, and thereby Reynolds number is an order of magnitude lower than for that seen on Earth, the lift curve (Fig 10) appears much more linear, while the trend in drag appears very similar to that in Earth atmosphere conditions. No inversed Magnus effect was resolved. The variation in predicted Strouhal number, plotted in fig 12, is minimal up to about  $\Omega = 2.0$  before fluctuations in the

lift and drag signal all but disappear, again indicating a suppression of wake shedding at spinning speeds higher than  $\Omega = 2.0$ .

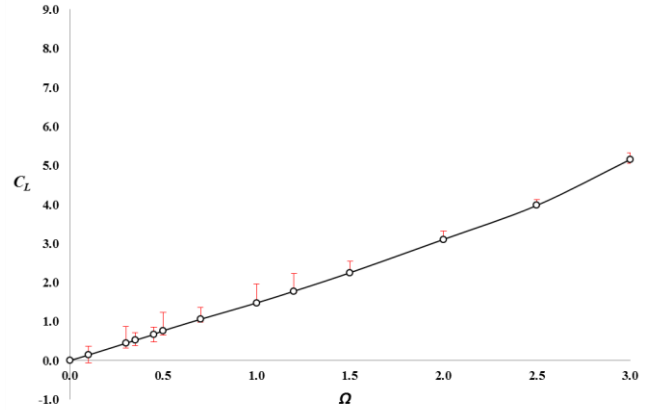


*Fig 10: Variation of  $C_L$  with  $\Omega$  for Mars surface conditions.  $U = 15\text{ m/s}$ .*

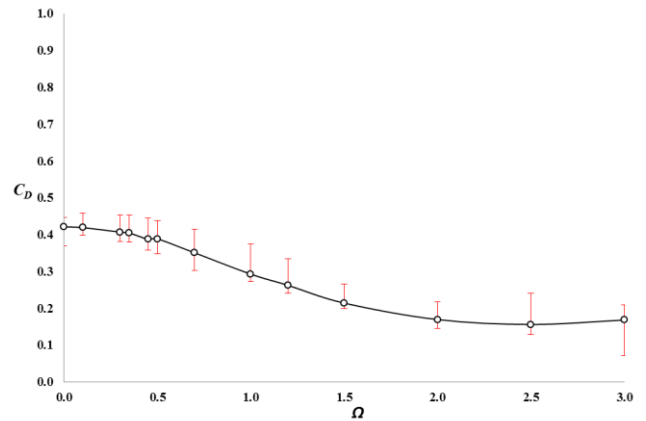


*Fig 11: Variation of  $C_D$  with  $\Omega$  for Mars surface conditions.  $U = 15\text{ m/s}$ .*

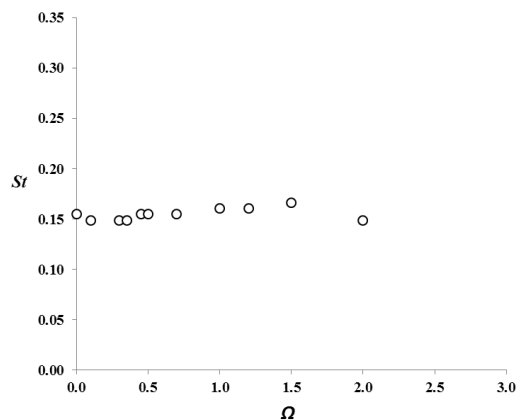
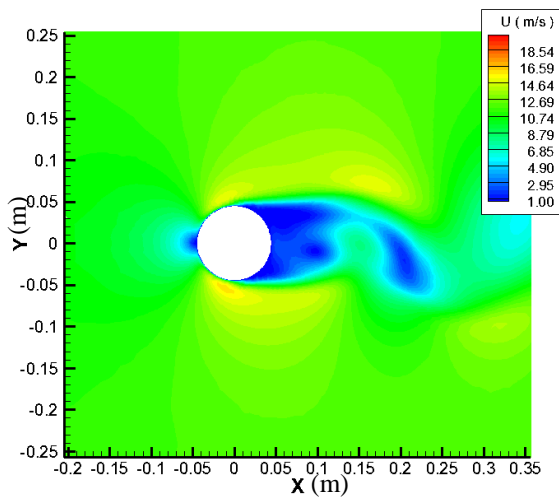
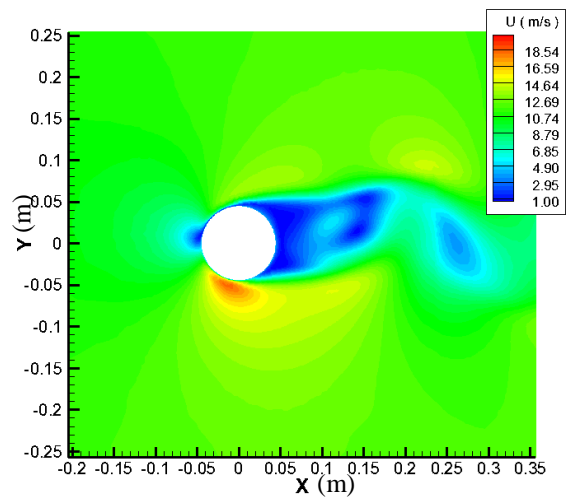


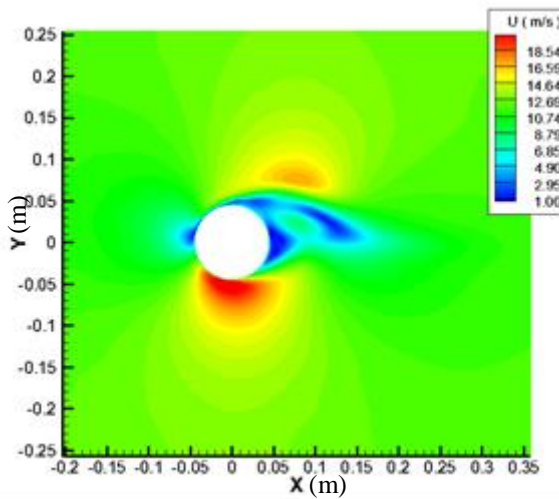
*Fig 12: Variation of shedding Strouhal number with  $\Omega$  for Mars surface conditions.  $U = 15\text{ m/s}$ .*



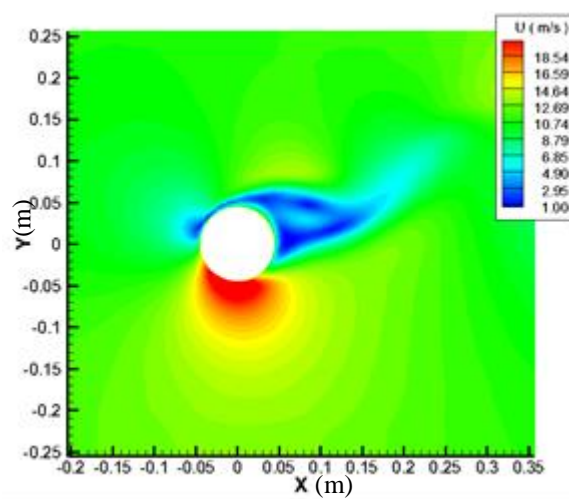
a)  $\Omega = 0.0$



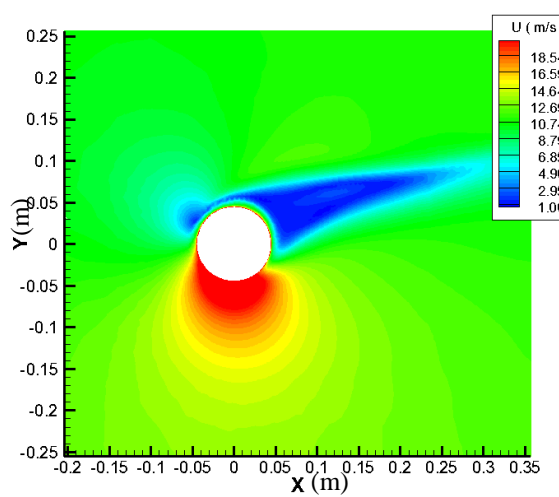
b)  $\Omega = 0.3$



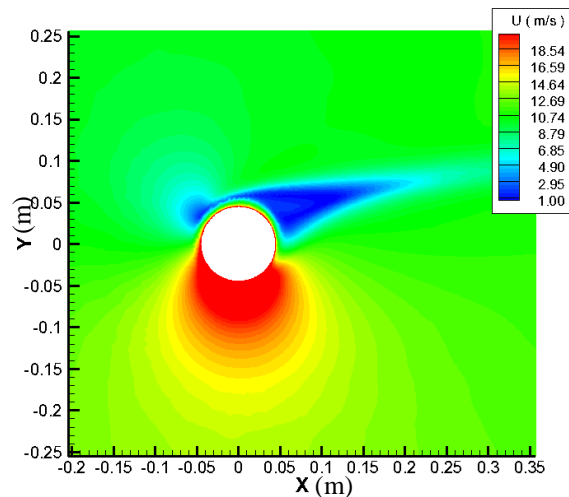
c)  $\Omega = 0.5$



d)  $\Omega = 1.0$



e)  $\Omega = 1.5$



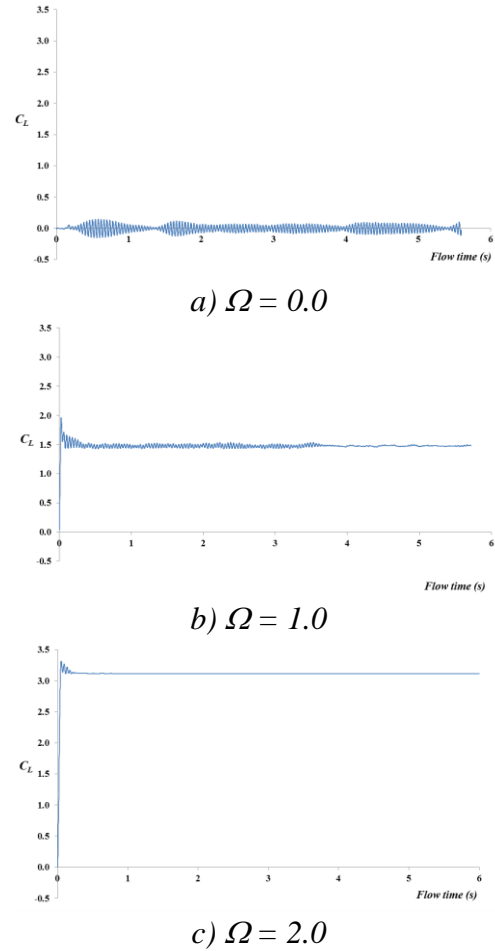
f)  $\Omega = 2.0$

Fig 13: Instantaneous contours of velocity magnitude at  $C_{Lmax}$ . Mars surface conditions,  $U=15\text{m/s}$ .

Fig. 13 presents the contours of instantaneous velocity magnitude at  $C_{Lmax}$  on the cylinder spanwise centre-plane, at a selection of the spinning speeds for the ground level conditions in the Martian atmosphere, corresponding to the same forward flight speed of 15m/s, as that investigated for Earth flight.

Here, the same trends in flow structure are evident as seen in the case of Earth conditions. A classic large low energy wake is evident with symmetric separation locations on the upper and lower cylinder surfaces, and a flow attachment zone seen at the windward symmetry line for  $\Omega = 0.0$ , together with evidence of large scale shed vortical eddies in the wake. With the introduction of cylinder spin, higher velocities, and hence lower pressures, are built up under the lower cylinder surface, than seen above the upper cylinder surface, and this is associated with an increasing asymmetry between the lower surface separation line (which is seen to move rearward) and the upper surface separation line (which is seen to move forward). The wake is seen to be deflected upwards for very high spinning speeds, and becomes closed with very little evidence of vortical shedding or significant fluctuation, in much the same manner as seen in the Earth condition simulations. Also evident are the relatively thick upper surface secondary laminar boundary layers, which are a result of the very low atmospheric density and temperature (very low Reynolds numbers).

Instantaneous force histories are plotted for three cylinder spinning speeds in fig 14. For the zero spinning case the average  $C_L$  is, as expected, zero, but there is a significant level of high frequency fluctuation ( $\sim 25\text{Hz}$ ) associated with the shedding of vortical structures, and a much lower frequency fluctuation around 1.5Hz, the origin of which requires more investigation. At  $\Omega = 1.0$  average  $C_L$  has risen to about 1.5 (higher than the corresponding value in Earth atmosphere conditions), and there has been a significant reduction in the level of fluctuation of lift force. At  $\Omega = 2.0$ ,  $C_L$  is around the level seen for corresponding spinning speed in Earth conditions, and there is now practically no fluctuation of  $C_L$  level at all.



*Fig 14:  $C_L$  time histories for three spinning speeds. Mars surface conditions.  $U = 15\text{m/s}$ .*

### 4.3 Simulations for Titanian Atmosphere, $Re_D = 39 \times 10^4$

Corresponding computed data for the variation of average lift and drag coefficient with  $\Omega$  in a simulated ground level atmosphere of Saturn's moon Titan, are plotted in fig. 15 and 16. Flight in the Titanian atmosphere, having a much thicker, high pressure but very low temperature condition at ground level, will be at much higher Reynolds number than seen at equivalent flight speeds on Earth or on Mars. In fact, the calculated value of  $Re_D = 39 \times 10^4$  puts the notional flow investigated here in the critical regime, where boundary layer transition prior to separation on the cylinder surface might be expected. At the higher spinning speeds it is suggested that the upper surface boundary layer (on the side opposing the flow of the

freestream) will transition first, with the associated separation line undergoing a sudden forward (upstream) movement. Such a phenomena could not be captured in the present numerical study, which models only a laminar cylinder surface boundary layer.

Fig 15 shows that the predicted average  $C_L$  remains close to zero until a spinning velocity ratio,  $\Omega$ , of 0.7, undergoing a minor inversion at  $\Omega \sim 0.3$ . Average  $C_L$  rises from  $\Omega=0.7$  until it reaches a plateau of  $C_L \sim 0.25 - 0.3$  beginning at a spinning speed of  $\Omega \sim 1.5$ . The variation of computed  $C_D$  with  $\Omega$  is plotted in fig 16. For the Titan surface conditions, predictions show that  $C_D$  varies with  $\Omega$  in the same trend as seen in the case of Earth and Mars surface conditions, but with much lower magnitude. The predicted wake shedding Strouhal number,  $St$ , is plotted against  $\Omega$  in fig 17. The trend for Titan conditions seems to resemble that seen for Mars conditions, displaying only small sensitivity to cylinder spinning speed, as opposed to the case of Earth surface conditions where a rise in spinning speed results in a rise in  $St$ .

Fig. 18 presents the contours of instantaneous velocity magnitude at  $C_{Lmax}$  on the cylinder spanwise centre-plane, at a selection of the spinning speeds for the ground level conditions in the Titanian atmosphere, corresponding to the same forward flight speed of 15m/s. Exactly the same physical flow features and trends with cylinder spinning speed are captured in this series of simulations as seen in those performed for Earth and Mars surface conditions. These include the development of separation line asymmetry, the formation of strong, extended regions of accelerated flow, and associated localized suction, on the lower surface which increase with spinning speed, the steady deflection upwards, and closure of the wake, and the suppression of the formation and shedding of large scale vortical structures into the wake above  $\Omega \sim 1.0$ .

The suppression of wake shedding is also evident in the computed  $C_L$  time histories, plotted in fig 19 for  $\Omega = 0.0, 1.0$  and  $2.0$ . Fluctuations in lift force are still evident at  $\Omega =$

1.0 and 2.0, but these are much less than those seen with the static cylinder.

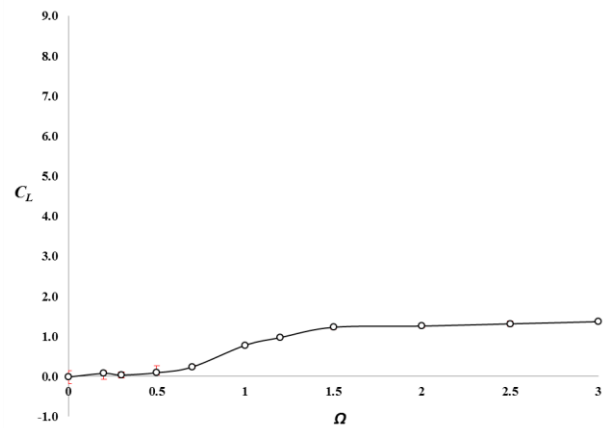


Fig 15: Variation of  $C_L$  with  $\Omega$  for Titan surface conditions.  $U = 15$  m/s.

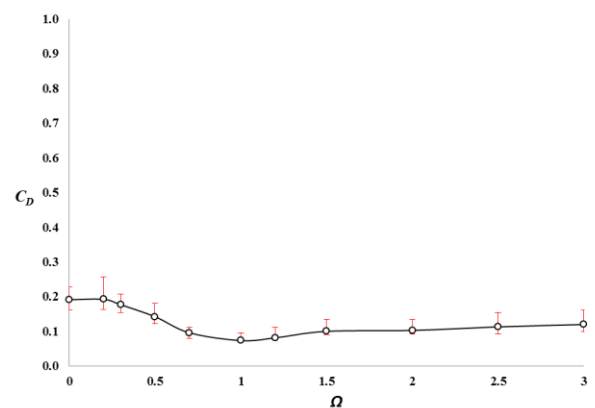


Fig 16: Variation of  $C_D$  with  $\Omega$  for Titan surface conditions.  $U = 15$  m/s.

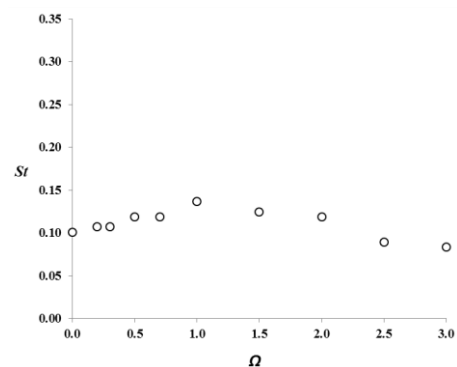


Fig 17: Variation of shedding Strouhal number with  $\Omega$  for Titan surface conditions.  $U = 15$  m/s.

**FEASIBILITY ASSESSMENT OF SPINNING CYLINDER LIFT FOR  
REMOTE FLIGHT IN MARS AND TITAN ATMOSPHERES**

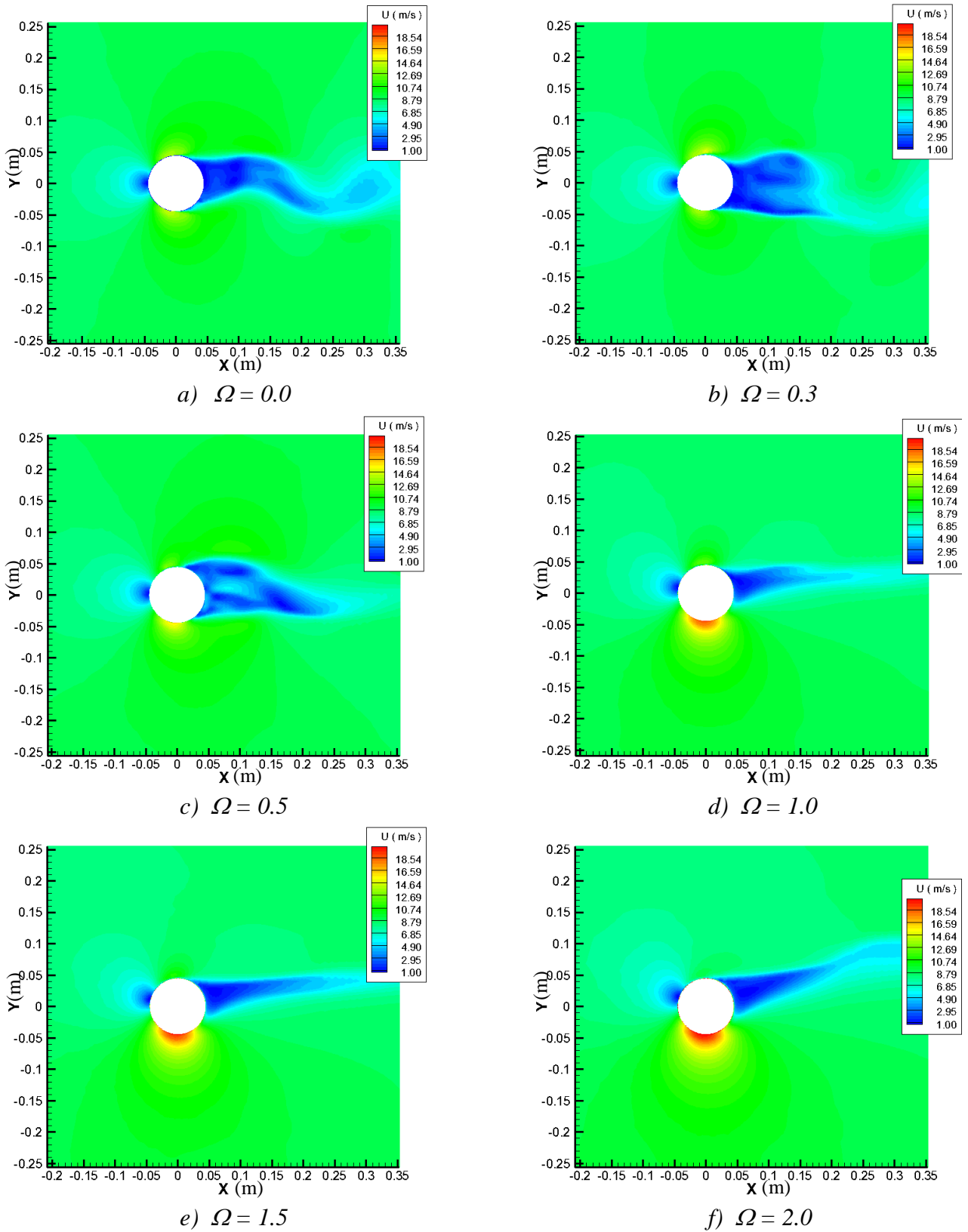


Fig 18: Instantaneous contours of velocity magnitude at  $C_{Lmax}$ . Titan surface conditions,  $U=15m/s$ .

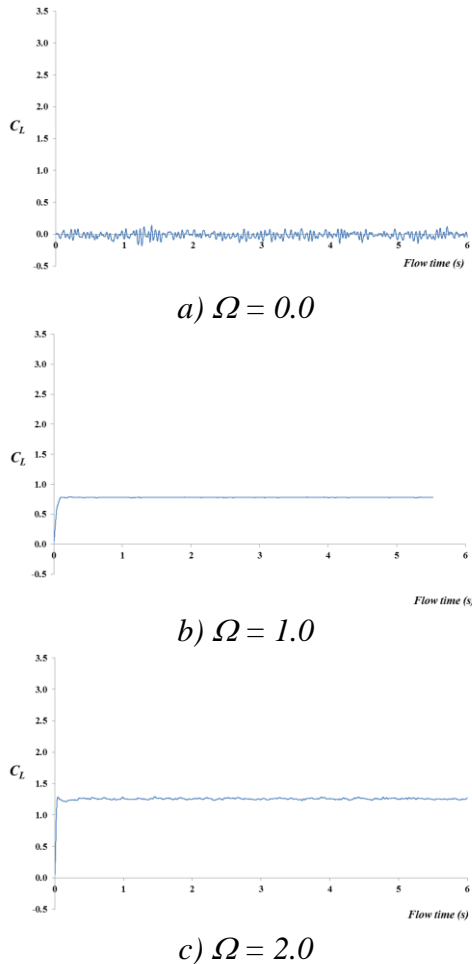


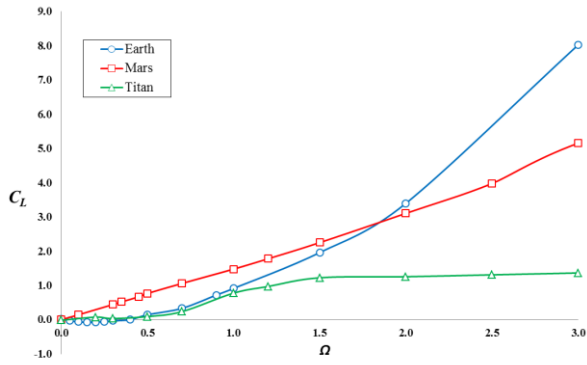
Fig 19:  $C_L$  time histories for three spinning speeds. Titan surface conditions.  $U = 15\text{m/s}$ .

The variation, with cylinder spinning speed, of average lift and drag coefficients and the lift to drag ratios are plotted in fig 20. The spinning cylinder is predicted to generate around the same level of  $C_L$  up to  $\Omega \sim 1.0$  in the Earth and Titan surface conditions, while at Mars surface condition, the spinning cylinder is predicted to deliver considerably higher levels of  $C_L$ . At  $\Omega \sim 2.0$  and above increasingly higher levels of  $C_L$  are predicted in Earth conditions, while the lowest  $C_L$  levels are generated in Titan conditions. Drag coefficient level is predicted to be highest on Earth, and lowest in the Titanian atmosphere. Comparing the lift to drag force ratio, which is a measure of the efficiency at which the lift force is generated, the spinning cylinder performance on Titan is better than that on Earth, up until  $\Omega > 2.0$ , where the data at  $\Omega = 3.0$  infers that  $L/D$  on Earth is slightly higher than on Titan. The highest  $L/D$ , at the highest

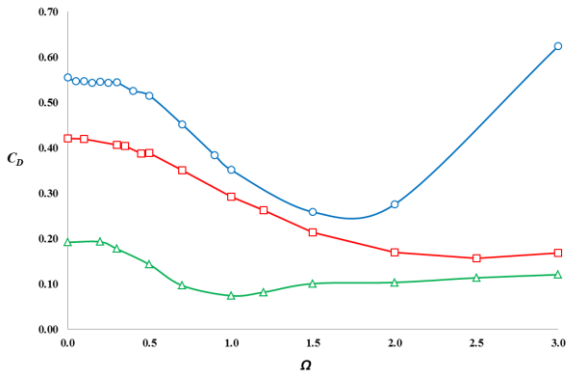
cylinder spinning speeds, is achieved in the Mars atmosphere.

For the assessment of the ability of a spinning cylinder lift based micro-UAV to carry a certain load at a constant  $U = 15\text{ m/s}$ , one also has to take into account the relative differences in the gravitational acceleration at the surface of these three worlds. The surface atmosphere of Mars may well be able to deliver the highest values of  $L/D$ , but the rarefied nature of the Martian atmosphere means that the lift force magnitude will be very small indeed.

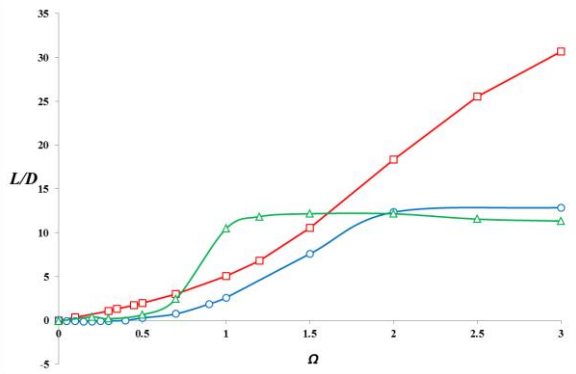
If we assume that we are interested in cruise performance at  $U = 15\text{ m/s}$ , where aerodynamic lift will equate to vehicle weight, and also make the assumption that all of the vehicle lift is generated by the spinning cylinder wings, we can infer the mass per unit cylinder span (also assuming perfect 2D lifting performance, which will obviously not be the case in reality), that the notional vehicle would be able to carry. Fig 21 compares the theoretical maximum mass per unit span, given these assumptions, that the notional vehicle would be able to carry in the surface level atmospheres on the three worlds of interest. We can see that spinning cylinder based lift can provide a much higher payload mass per unit wing span in the Titanian environment than on Earth. Spinning cylinder lift is not viable for a micro-UAV vehicle on Mars, in spite of its aerodynamic efficiency, due to its very low density, and this impediment would also affect a fixed wing based craft. It is suggested that a spinning cylinder lift based micro-UAV vehicle might be feasible as a means to explore the Titanian surface environment if a means for power generation (not from the Sun which is too far away for solar power harvesting to be feasible) would be devised for the landing launch platform, which would incorporate an arm to pick up the nearby UAV after it lands, and a docking port for electrical power transfer, and a catapult launch system.



a)  $C_L$  versus  $\Omega$



b)  $C_D$  versus  $\Omega$



c)  $L/D$  versus  $\Omega$

Fig 20: Comparison of variation of aerodynamic forces for  $U=15\text{m/s}$  forward flight in the three surface atmosphere conditions.

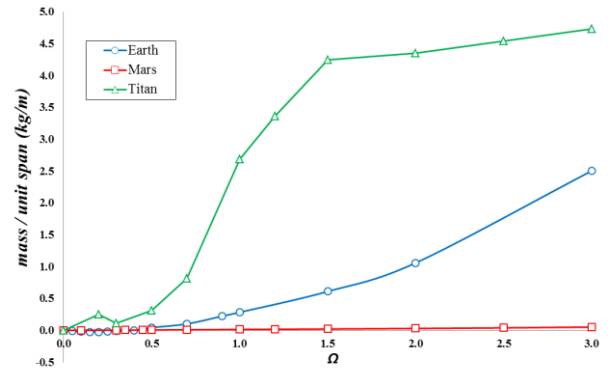


Fig 21: Comparison of variation of maximum vehicle mass based on finite span spinning cylinder lift, for  $U=15\text{m/s}$  forward flight in the three surface atmosphere conditions.

## 5 Conclusions

This study has derived the following conclusions:

- Modern computational methods for the solution of the laminar unsteady Navier-Stokes equations can successfully capture the physical trends and magnitudes of the lift and drag, and the viscous flow physics associated with static and spinning cylinders in sub-critical Reynolds number crossflows.
- The method, applied to a spinning cylinder, at different surface to freestream velocity ratios, for  $U=15\text{m/s}$  freestream in the Earth, Mars and Titan surface atmosphere conditions, suggests that a spinning cylinder lift based micro-UAV might be feasible as a vehicle for the exploration of the Titanian surface, but would not be feasible for similar application in the very rarefied atmosphere of Mars.

## References

- [1] Robins, B. "New Principles of Gunnery", London, UK. 1742.
- [2] Magnus, G. "On the Deflection of a Projectile", *Poggendorf's Annalen der Physik und Chemie*, Vol. 88, 1853, pp. 804-810.
- [3] Lord Rayleigh, "On the Irregular Flight of a Tennis Ball", *Scientific Papers*, Vol. 1, 1857, pp. 344-346.

- [4] Prandtl, L. & Tietjens, O. “Applied Hydro- and Aeromechanics”, McGraw-Hill Book Company Inc., New York, 1961, pp. 80-85.
- [5] Lafay, M. A. “Sur l’Inversion du Phenomene de Magnus” *Comptes-Rendus*, Vol. 151, 1910, pp. 417-442.
- [6] Lafay, M. A. “Contribution Experimentale a l’Aerodynamique du Cylindre” *Revue Mecanique*, Vol. 30, 1912, pp. 417-442.
- [7] Reid, E. G. “*Tests of Rotating Cylinders*”, Technical Report TN-209, NACA, 1924.
- [8] Thom, A. “*The Aerodynamics of a Rotating Cylinder*” PhD Thesis, University of Glasgow, UK, 1926.
- [9] Thom, A. “*Experiments on the Air Forces on Rotating Cylinders*”, Technical Report R&M No. 1018, Aeronautical Research Council, 1925.
- [10] Thom, A. “*The Pressures Round a Cylinder Rotating in an Air Current*”, Technical Report R&M No. 1082, Aeronautical Research Council, 1926.
- [11] Thom, A. & Sengupta, S. R. “*Air Torque on a Cylinder Rotating in an Air Stream*”, Technical Report R&M No. 1410, Aeronautical Research Council, 1931.
- [12] Thom, A. “*Effects of Discs on the Air Forces on a Rotating Cylinder*”, Technical Report R&M No. 1623, Aeronautical Research Council, 1934.
- [13] Swanson, W. M. “The Magnus Effect: A Summary of Investigations to Date”, *Journal of Basic Engineering*, Vol. 83, 1961, pp. 461-470.
- [14] Badalamenti, C. “*On the Application of Rotating Cylinders to Micro Air Vehicles*”, PhD Thesis, City University London, UK, 2010.
- [15] Gowree, E. R. & Prince, S. A. “A Computational Study of the Aerodynamics of a Spinning Cylinder in a Crossflow of High Reynolds Number” *Proceedings of the 28<sup>th</sup> International Congress of the Aeronautical Sciences*, Brisbane, Australia, Paper 245, 2012.
- [16] Zdravkovich, “*Flow Around Circular Cylinders, Volume 1: Fundamentals*”, Oxford University Press Inc., New York, 1997.

copyright holder of this paper, for the publication and distribution of this paper as part of the ICAS 2014 proceedings or as individual off-prints from the proceedings.

### Email Address

mailto: simon.prince@cranfield.ac.uk

### Copyright Statement

The authors confirm that they, and/or their company or organization, hold copyright on all of the original material included in this paper. The authors also confirm that they have obtained permission, from the copyright holder of any third party material included in this paper, to publish it as part of their paper. The authors confirm that they give permission, or have obtained permission from the